Geophysical Journal International

Geophys. J. Int. (2017) **210,** 979–988
Advance Access publication 2017 May 26
GJI Seismology

doi: 10.1093/gji/ggx204

Source characteristics and geological implications of the January 2016 induced earthquake swarm near Crooked Lake, Alberta

Ruijia Wang,[1] Yu Jeffrey Gu,[1] Ryan Schultz,[2] Miao Zhang[3] and Ahyi Kim[4]

[1] *Department of Physics, University of Alberta, Edmonton, Alberta, Canada. E-mail: ruijia3@ualberta.ca*
[2] *Alberta Geological Survey, Edmonton, Canada*
[3] *Earth and Environmental Sciences Division, Los Alamos National Laboratory, Los Alamos, NM, USA*
[4] *Department of Material System Science, Yokohama City University, Yokohama City, Japan*

Accepted 2017 May 25. Received 2017 May 8; in original form 2017 March 27

SUMMARY

On 2016 January 12, an intraplate earthquake with an initial reported local magnitude (M_L) of 4.8 shook the town of Fox Creek, Alberta. While there were no reported damages, this earthquake was widely felt by the local residents and suspected to be induced by the nearby hydraulic-fracturing (HF) operations. In this study, we determine the earthquake source parameters using moment tensor inversions, and then detect and locate the associated swarm using a waveform cross-correlation based method. The broad-band seismic recordings from regional arrays suggest a moment magnitude (**M**) 4.1 for this event, which is the largest in Alberta in the past decade. Similar to other recent **M** $\sim$ 3 earthquakes near Fox Creek, the 2016 January 12 earthquake exhibits a dominant strike-slip (strike $=$ 184°) mechanism with limited non-double-couple components ($\sim$22 per cent). This resolved focal mechanism, which is also supported by forward modelling and P-wave first motion analysis, indicates an NE–SW oriented compressional axis consistent with the maximum compressive horizontal stress orientations delineated from borehole breakouts. Further detection analysis on industry-contributed recordings unveils 1108 smaller events within 3 km radius of the epicentre of the main event, showing a close spatial-temporal relation to a nearby HF well. The majority of the detected events are located above the basement, comparable to the injection depth (3.5 km) on the Duvernay shale Formation. The spatial distribution of this earthquake cluster further suggests that (1) the source of the sequence is an N–S-striking fault system and (2) these earthquakes were induced by an HF well close to but different from the well that triggered a previous (January 2015) earthquake swarm. Reactivation of pre-existing, N−S oriented faults analogous to the Pine Creek fault zone, which was reported by earlier studies of active source seismic and aeromagnetic data, are likely responsible for the occurrence of the January 2016 earthquake swarm and other recent events in the Crooked Lake area.

Key words: North America; Earthquake dynamics; Earthquake source observations; Fractures, faults, and high strain deformation zones; Mechanics, theory, and modelling; Transform faults.

1 INTRODUCTION

Earthquakes associated with anthropogenic activities in the Western Canada Sedimentary Basin (WCSB), most notably in the Horn River Basin (B.C. Oil and Gas Commission 2012), Montney Formation (B.C. Oil and Gas Commission 2014; Babaie Mahani *et al.* 2017), Cordel Field (Schultz *et al.* 2014), near Cardston (Schultz *et al.* 2015a), Rocky Mountain House (Wetmiller 1986; Wang *et al.* 2015) and Crooked Lake (Schultz *et al.* 2015b; Bao & Eaton 2016; Clerc *et al.* 2016; Deng *et al.* 2016; Schultz *et al.* 2017), have garnered significant scientific interest and public attention in the past 3 yr. While the vast majority of these earthquakes could only be detected by sensitive seismic instruments, several events with moment magnitudes close to **M**4 were felt hundreds of kilometres away (e.g. 280 km, CBC 2016; Globalnews 2016) and have been linked to nearby HF operations (Schultz *et al.* 2017). In the Fox Creek/Crooked Lake region alone, the number of **M** $>$ 3 earthquakes increased from 3 over a 28 yr period prior to November 2013 to 35 in the last 4 yr (December 2013–February 2017) (Earthquakes Canada). The first moderate earthquake (**M**3.6) occurred in January 2015 (Bao & Eaton 2016), which was accompanied by hundreds of smaller events and became the catalyst in the drafting of the 'traffic-light' protocol for completion operations in the Duvernay Formation in this region (Alberta Energy Regulator 2015). Since

then, two events have triggered the stoplight in compliance with this regulation, including the local magnitude (M_L) 4.8 (Alberta Geological Survey, AGS) earthquake on 2016 January 12 near Crooked Lake, which is the largest in Alberta, Canada in the past decade.

The January 12 earthquake raises many critical questions pertaining to the seismic hazard assessment of shale gas development in the WCSB. For example, examination of the nature of surrounding earthquakes relies on accurate determinations of the source locations as well as their temporal relationship to nearby industry (e.g. Holland 2013; Skoumal *et al.* 2015). To understand the relationships among earthquakes, industry activities, and the geological framework, source parameters of the January 12 earthquake are critical.

In this paper, we present an integrated source analysis for the 2016 January 12 earthquake with data both from the regional seismic arrays and from a small network of four near-source stations contributed by the industry. For simplicity, we will refer to the largest event occurring on 2016 January 12 near Crooked Lake as the J12EQ hereinafter. Based on existing geological information and the distribution of the detected earthquake swarm, we are able to (1) determine the true fault orientation and place it in the regional geological context, and (2) establish the connection between the seismicity and the nearby HF activities. Our study suggests that the J12EQ is representative of the majority of HF related earthquakes (i.e. eight $\mathbf{M} > 3$ earthquakes in late 2016) around the Crooked Lake region, and the new information on the source properties could greatly benefit future analyses of natural and induced earthquakes in the WCSB.

Since the contribution of anthropogenic activities on the stress release cannot be evaluated statistically, it is difficult to unequivocally differentiate between 'triggered' and 'induced' earthquakes (Dahm *et al.* 2013). The former term has been associated more frequently with naturally occurring, remote events that take place within short time intervals (Wang *et al.* 2015; Fan & Shearer 2016). Following the convention of recent studies (Ellsworth 2013; Rubinstein & Mahani 2015; Atkinson *et al.* 2016; Ghofrani & Atkinson 2016), this study will simply refer to earthquakes associated with human activities as 'induced'.

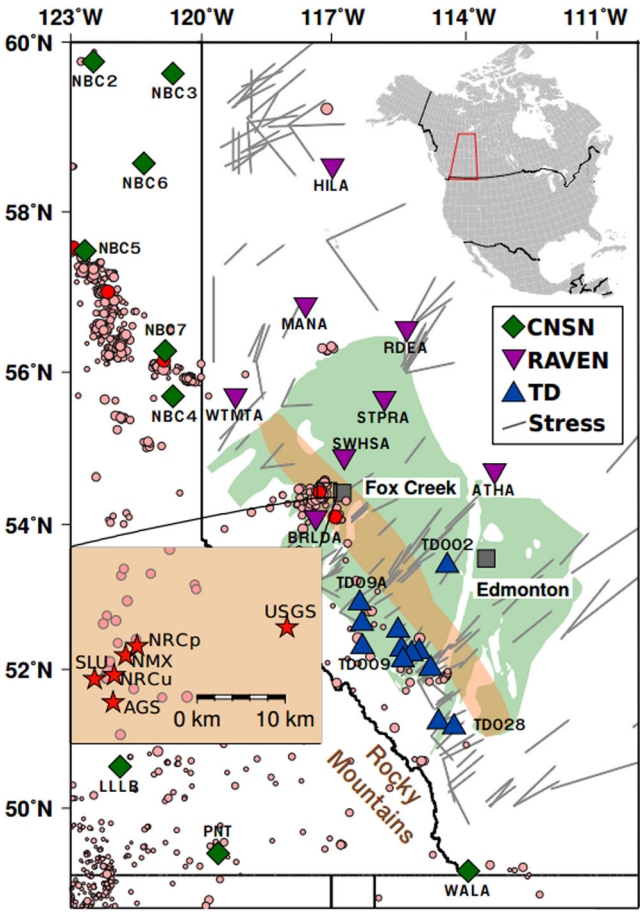

Figure 1. Spatial distribution of seismic monitoring stations and earthquakes (circles) since 2013; $\mathbf{M} > 4$ earthquakes are shown in red. The area of occurrence of the Duvernay Formation is shaded in light green, with the wet-gas region highlighted in yellow (Rokosh *et al.* 2012). Crustal stress orientations obtained from borehole breakouts are shown by the grey lines. The map inset shows the epicentres of the J12EQ reported by different agencies (red stars): U. S. Geological Survey (USGS); Nanometrics Athena (NMX); Saint Louis University Earthquake Center (SLU); Alberta Geological Survey (AGS); Natural Resources Canada (NRC), where 'p' and 'u' indicate the previous and updated locations, respectively.

2 STUDY REGION AND DATA

A number of recent studies (Bao & Eaton 2016; Clerc *et al.* 2016; Schultz *et al.* 2017) indicated that the majority of the seismicity (including the J12EQ) in Alberta since 2013 was located near the northwestern wet-gas section of the Duvernay Formation (Fig. 1). Since 2013, multistage HF operations, which require the drilling of horizontal wells and injection of fluid mixture underground, have been widely utilized in this region (Schultz *et al.* 2015b; Atkinson *et al.* 2016; Wang *et al.* 2016). While shale permeability is greatly enhanced through the opening of fractures accompanied by microseismicity ($\mathbf{M} < 0$), HF has been linked to a substantial increase in seismicity rate since 2013 (Schultz *et al.* 2017), as well as several **M**1.7–3.9 earthquakes (Holland 2013; Atkinson *et al.* 2014; Wang *et al.* 2016). Provincial protocols (Alberta Energy Regulator 2015) have been established and twice led to temporary suspensions of HF operations in the Duvernay Formation.

The hypocentre of the J12EQ is located approximately 30 km west of Fox Creek, Alberta (Fig. 1). The depths reported by several agencies vary between 3–8 km, overlapping with the depth of the Precambrian crystalline basement (3.8 km, Pilkington *et al.* 2000; Majorowicz *et al.* 2014). Early sedimentation in this area occurred in a marine environment, resulting in the Beaverhill Lake Group and Elk Point Group carbonates, shales, and evaporites underlying the Duvernay Formation (Switzer *et al.* 1994). The Duvernay Formation is a late Devonian aged (~370 Ma), organic-rich, silica-rich stratigraphic unit within the Woodbend Group at an approximate depth of 3 km (Wendte & Uyeno 2005). The thickness of the Duvernay Formation varies mainly between 25 and 60 m in a broad region covering ~56 000 km^2 in total area, where ~24 000 km^2 is within the wet-gas or volatile-oil maturity window (Dunn *et al.* 2012; Davis & Karlen 2013). Much of the mature area is overpressured with a pressure-depth ratio reaching 19 kPa m^{-1} (Fox & Soltanzadeh 2015).

Our data set contains three-component recordings of the J12EQ from three regional telemetered networks: TransAlta Dam Monitoring Network (TD), Canadian National Seismograph Network (CNSN) and the Regional Alberta Seismic Observatory for Earthquake Studies Network (RAVEN; Schultz & Stern 2015; Fig. 1). The distances of the selected stations from the epicentre range from 30 to 700 km, providing relatively uniform coverage except an azimuth gap of 86° towards the NW. After the removal of

instrument responses, we integrate the original velocity seismograms to displacement and rotate the source–receiver paths to the great circle. Based on the signal-to-noise ratios of the recorded waveforms, 24 out of 29 stations are retained after quality control. Finally, the swarm associated with the J12EQ is detected with the continuous waveform data from four near-source (<10 km) stations recently made public by industry operators.

3 METHOD

To compute the Green's functions we adopt a 1-D velocity model consisting of 14 layers. The upper crust in this model is modified from Welford & Clowes (2006) based on an active source experiment. The lower crustal velocity model is taken from a recent receiver function analysis (Chen *et al.* 2015) beneath station PER (Gu *et al.* 2011). The attenuation model is modified from Zelt & Ellis (1990) by Wang *et al.* (2016) and the forward waveforms are computed using a frequency wavenumber integration approach (Saikia 1994). For a detailed analysis of the effects of model perturbations on moment tensor solutions, which are mostly secondary, we refer the reader to Wang *et al.* (2016).

Full moment tensor solutions are obtained from time domain inversions based on the TDMT_INV package (Dreger 2003). Improvements were made to the original package to enable the simultaneous inversion of multiple frequencies, data channels, and phases. A low-frequency range (0.05–0.1 Hz) is chosen for surface-waves and a slightly higher-frequency (0.08–0.4 Hz) range is used to emphasize the body-wave constraints. We vary the weights of the individual waveforms based on both source-station distance and the relative amplitude in the corresponding frequency ranges. To compare and validate the inversion results, we determine pure double-couple (DC) moment tensors from forward modelling (Kim *et al.* 2011) by searching over all possible strike, dip, and rake angles with a uniform step size of 5 degrees. To evaluate the quality of waveform fitting during the inversion and forward simulations, we define the variance reduction (VR) as

$$VR = \left[1 - \frac{\sum_{i=1}^{m}(d_i - s_i)^2}{\sum_{i=1}^{m} d_i^2}\right] \times 100\% \quad (1)$$

where d_i and s_i are the ith elements of the concatenated data and synthetic time series, respectively. The maximum dimension m is the total number of time samples from all components (3), frequency bands (2), and stations. The VR is also used to compare the results from different locations as well as to determine the best focal depth. While all stations from 30 to 700 km are used to resolve the full moment tensor, we only consider data recorded by regional stations within 250 km during the location and depth searches to ensure sufficient sensitivities to the hypocentral location.

Since the Green's functions are only calculated based on a 1-D velocity model, it is useful to introduce time shifts to the three-component waveforms of a given station to minimize the effect of (1) uncertain source location, (2) inaccurate velocity model, and (3) path heterogeneity among stations. After the waveforms are adjusted optimally (VR > 70 per cent), the transverse, radial, and vertical components for each station are shifted independently to further improve the fit and minimize the potential effects of anisotropy (Frohlich 1994; Vavryčuk *et al.* 2008). The latter shifts are secondary, typically within 1 s and smaller than the shortest half period (1.25 s). Effects associated with path uncertainty and heterogeneity have been tested in Wang *et al.* (2016) for a comparable case study and the influence of anisotropy, especially around the Duvernay Formation, will be detailed in Section 4.1.

4 RESULTS

4.1 Magnitude and focal mechanism solution

The moment tensor solution obtained from the J12EQ produces excellent waveform matches to the recordings from regional (30–700 km) stations (Fig. 2a). This solution is predominately strike-slip with N–S and E–W oriented fault planes, consistent with solutions obtained from forward simulations (inset, Fig. 2a). It also resembles the focal mechanisms for other events within the Crooked Lake region (further discussed in Section 5). It is worth mentioning that the moment magnitude is independently obtained during full moment tensor inversions and forward modelling (Section 3). Both methods yield a value of **M**4.1, which is consistent with the moment magnitude from SLU (**M**4.14), but smaller than the other reported values (**M**4.4, NRC; M_L4.8, AGS; M_L4.9, NMX). The decomposed moment tensors at various locations suggest a strong DC component (up to 80 per cent), while only minor non-DC [a horizontal compensated-linear-vector-dipole (CLVD) and <5 per cent isotropic] may be needed to match the waveform data.

We adopt a bootstrap resampling test (Efron & Tibshirani 1991) to quantify the uncertainties in the source solution. To accomplish this, we first divide the original data into subsets based on source-station distances or azimuths, and then automatically determine the strike, slip and rake angles (Fig. 3) from randomly selected subsets containing 70 per cent of the data. This procedure is repeated 200 times to produce a statistically significant distribution of each parameter (Wang *et al.* 2016). The outcomes of the bootstrap resampling tests show consistent fault orientations and the standard deviations of the Gaussian-like distributions are no greater than 4°.

A further validation of the focal mechanism is provided by the observed *P*-wave first motion (Fig. 2a; Udías *et al.* 2014). In this analysis we carefully determine the first motions from the vertical-component waveforms of 24 regional stations (Fig. 1) and four near-source stations (Fig. 5) within the frequency range of 0.5–5 Hz. The take-off angles are calculated from the same velocity model presented in Section 2. Nearly all of the identified first motions are consistent with the focal mechanism from moment tensor inversion (Fig. 2a).

This source solution is stable within minor perturbations in sediment and bedrock velocities (Wang *et al.* 2016). One further consideration is the effect of seismic anisotropy, which is known to exist in the sedimentary layers and may introduce errors to forward modelling and inversions (Vavryčuk *et al.* 2008) when stations from wide azimuths and far offsets are used. It has been suggested that the crustal anisotropy is mostly aligned along an SW–NE orientation in the WCSB (Saruwatari *et al.* 2001; Fouch & Rondenay 2006). The amount of anisotropy for the Duvernay shale ranges from 25 per cent to 35 per cent for both *P* and *S* waves at a confining pressure of 90 MPa, as was determined from core samples (Ong *et al.* 2016), but the overall effect of anisotropy within the thin shale layer (25–60 m) is minor (∼5 per cent, Saruwatari *et al.* 2001) in view of the scale length of the source-receiver paths (30–700 km). This is corroborated by the consistent resulting source mechanisms with (Fig. 3) and without (Supporting Information Figures S1 and S2) the secondary time shifts detailed in Section 3. The VR increased by 5 per cent, but the fault angles changed by less than 12°

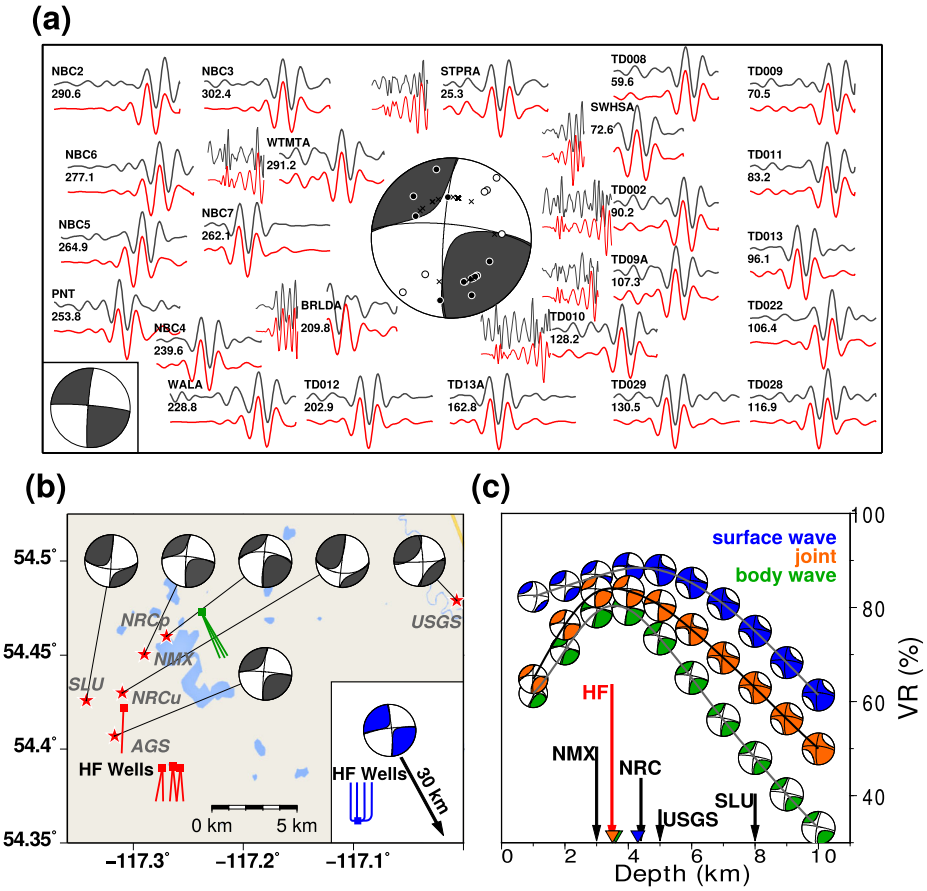

Figure 2. (a) Moment tensor solution, observed (grey) and best-fit synthetic (red) vertical-component waveforms. Station names and the corresponding azimuths are labelled near the observed waveforms. High-frequency body waves are also used and displayed for stations within 250 km (to the left of the low-frequency waveforms). The circles on the focal mechanism indicate compressional (filled black) and dilatational (filled white) *P*-wave first motions picked from vertical-component waveforms (including industry contributed stations). The crosses indicate unknown first motions due to low signal-to-noise ratios in *P* arrivals. The focal mechanism from pure-DC modelling is shown in the lower left corner. (b) Inversion results for different epicentres and the potentially responsible HF wells with drilling completed in early (green) and late (red) 2015. The focal mechanism for the 2015 June 13 earthquake (Wang et al. 2016) is presented in the lower right corner with the corresponding HF wells (blue). (c) Depth search using different input data. The black arrows indicate the available focal depths reported by different agencies and the red arrow indicates the injection depth of HF operations in the source area.

after secondary shifts were applied to minimize the effect of seismic anisotropy.

4.2 Hypocentre location of the J12EQ

The VR values from moment tensor inversion also provide an effective means to refine the location of this earthquake. Six hypocentral locations from five different agencies have been reported for the J12EQ near Fox Creek (Fig. 1). Most of the locations vary within 5 km except the epicentre reported by USGS, which is roughly 15 km east from the averaged centre of the other reported locations. The considerable scatter of the reported locations may be attributable to the use of different regional crustal models and stations/networks. To improve the accuracy of the source location, we perform full moment tensor inversions using the same local stations (<250 km) for all possible epicentres with a fixed depth of 4 km (Fig. 2b). Minor variations in fault plane angles (i.e. strike, slip and dip) are obtained from the output parameters based on different input locations. We observe large variations in the percentage of non-DC component: for example, the USGS source location renders high CLVD components (66 per cent), which contrasts with the DC-dominated focal mechanisms inverted from other starting locations. Our preferred epicentre is selected based on a comparison of VR values (Supporting Information Table S1). As the result, the hypocentral location reported by NRCu achieved the highest initial VR of 82.11 per cent, though the optimal solution converges on the location reported by NMX (VR = 85.03 per cent, Fig. 2a) after additional adjustments (e.g. time shifts, Section 2); this location is 3–6 km from seven potentially associated HF wells (Fig. 2b). The final focal depth is determined through a grid search from 1 to 10 km (Fig. 2c) at the NMX reported epicentral location. Through independent depth-search analyses on the body waves, surface waves and the combination of the two, we determine the optimal hypocentral depth range to be 3.5–4.3 km (Fig. 2c). The hypocentral location and depth are further refined using four operator contributed stations within 10 km of the HF wells during the detection of multiples (Section 4.3).

4.3 Detection and location of the earthquake swarm

The availability of injection parameters (Fig. 4) and near-source broadband data contributed by the operator (stations WSK01–04,

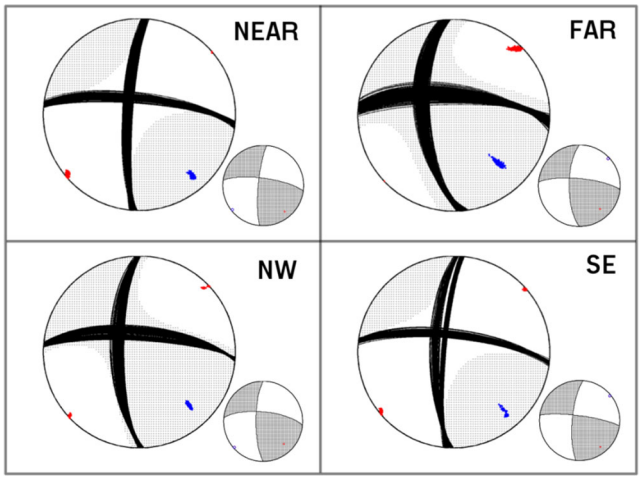

Figure 3. Bootstrap resampling tests of the inversion stability using the following four subsets of the recordings: near source stations (30–250 km); far source stations (250–700 km); azimuth between 235° (i.e. −125°) to 45° (NW); azimuth between 45° to 235° (SE). Seventy per cent of the stations from each group are used during bootstrapping and the black lines show the corresponding fault planes from 200 trials. The corresponding results from forward simulations are also shown. The red and blue dots mark the corresponding *P*- and *T*-axes from each solution.

Fig. 5) enable a detailed examination of the seismicity leading to, and immediately following, the J12EQ. We adopt 15 events with $M_L > 2$ (reported by Earthquakes Canada and AGS, Schultz *et al.* 2017), including the J12EQ, as master events and systematically search for potential repeating earthquakes within 3 km of the suspected well using the match and locate method (from here on, M&L, Zhang & Wen 2015a). Unlike the traditional template matching method which assumes that the template event and slave event are collocated or sufficiently close, M&L scans over potential event locations around the template, by making relative travel-time corrections based on the relative locations of the template event and the potential event before their cross-correlogram stacking (Zhang & Wen 2015a, b). In our analysis, only *S*-wave phases with the relatively large amplitudes are used. The search space is divided into uniform grids with the respective dimensions of 300 and 100 m in hypocentral location and depth. It should be noted that, events after January 19, 2016 are not detected due to the short duration of the accessible data.

Our analysis resulted in 1108 detected events with waveform cross-correlation coefficients (CC) larger than 0.3, a detection criterion chosen empirically. Among the robustly detected events (CC > 0.5, 454), not a single event was detected before the stimulation (Fig. 4b) that started on January 4 and ended at 11:34am (MTZ) on 2016 January 12. The majority (63.44 per cent) of the detected events were concurrent with the 26 stages of hydraulic fracturing, during which the cumulative seismic moment and cumulative injected volume closely tracked one another. Both the number of events and the daily maximum magnitude decreased during the post completion period, and the last stage of the injection is marked by the occurrence of the J12EQ (7 min before the end of the 26th stage).

To assess the likelihood of a temporal association between the rate of earthquakes and the injected volume, we conducted a cross-correlation reshuffling test (Telesca 2010). The result of this test suggests a statistical confidence greater than 99.99 per cent that the newly detected events from M&L are correlated with the completions of the southern well in this three-well pad (Fig. 5). The temporal (and spatial) correlation between seismicity and injection activities is critical in assessing the cause of the January 2016 earthquake swarm.

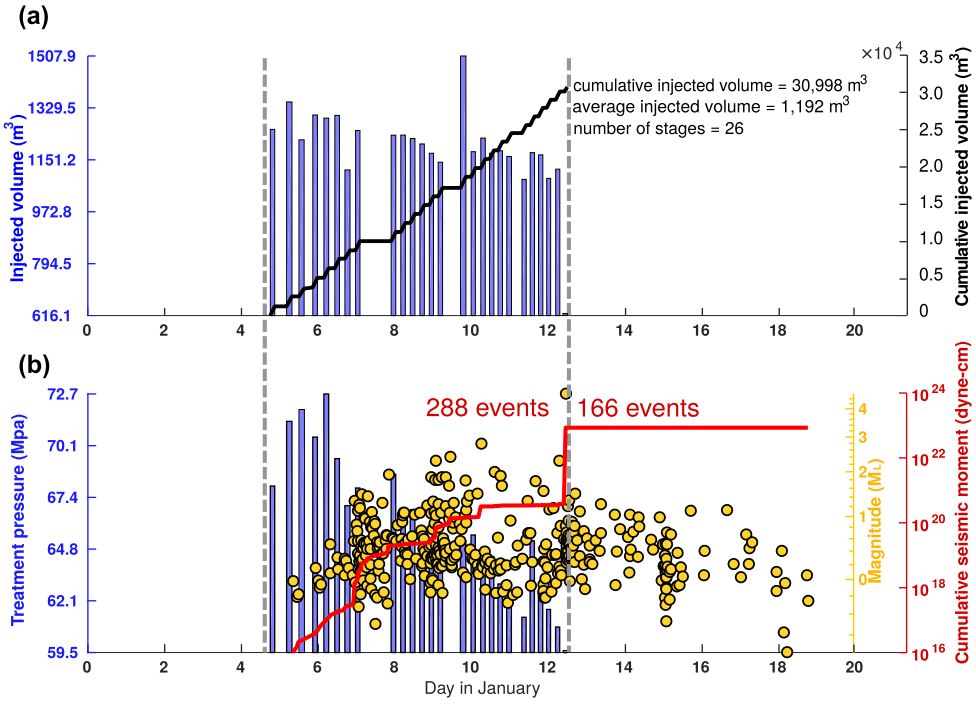

Figure 4. (a) Injection at the HF well (well ID: 100/15–25-062–23W5/00). Each bar represents a single HF stage and the cumulative volume is shown by the solid black line. (b) Similar to (a) but for treatment pressure at each stage. Superimposed on the plot are the detected multiples (yellow circles) with CC > 0.5 and the cumulative seismic moment (red line). The grey dash line in both plots marks the period of HF stimulation (2016 January 4 to 12). The largest event occurred during the last stage of stimulation, followed by a decrease in seismicity rate.

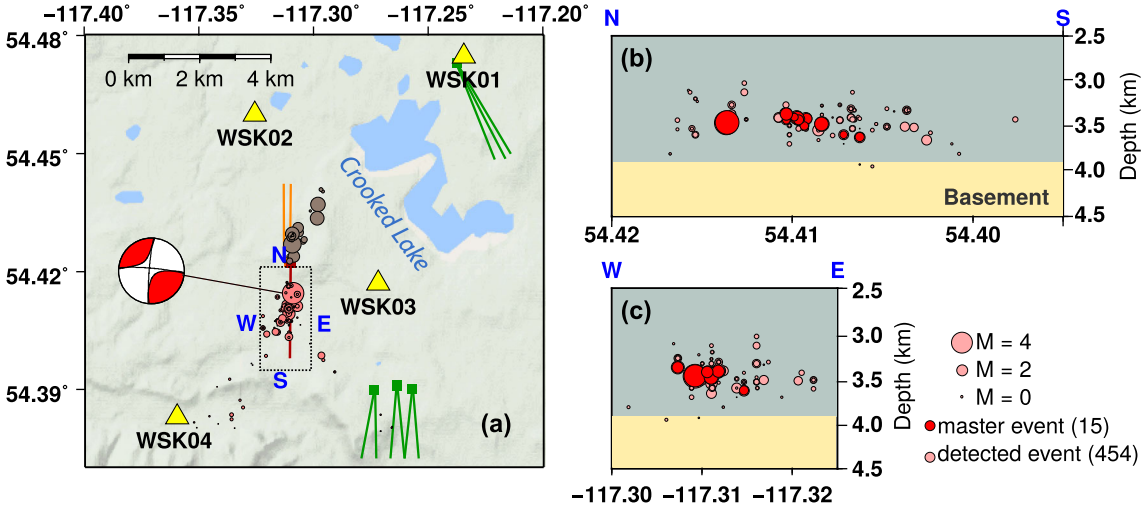

Figure 5. (a) Locations of the January swarm (red, CC > 0.5) detected using data from four industry-contributed stations (yellow triangles). The HF well associated with the January 2016 earthquake swarm is shown by the red line and the wells associated with an earlier swarm (brown, January 2015) are shown in orange (Bao & Eaton 2016; Schultz *et al.* 2017). Other active wells in 2015 and 2016 are shown in green. (b,c) Cross-sectional views of the detected events from the swarm within the dash box shown in (a). Some events are overlapped due to the limited size of the search grid.

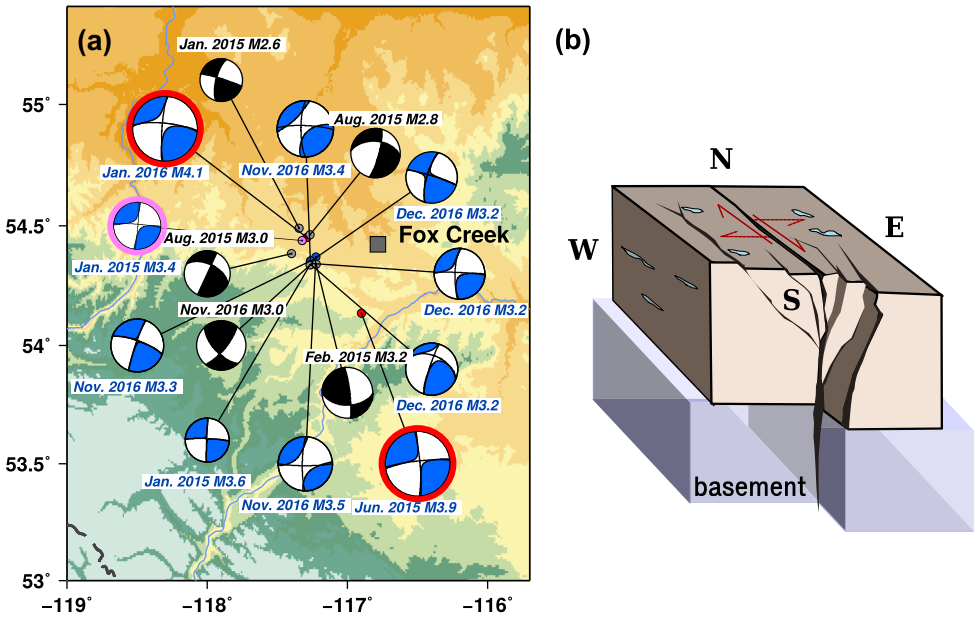

Figure 6. (a) A summary of the resolved focal mechanism and moment magnitude of earthquakes around Fox Creek. The event that triggered the 'traffic-light' protocol is highlighted in pink and the two red-light cases are highlighted in red. Focal mechanisms are resolved from double-couple forward modelling (black) when the data quality is insufficient for full moment tensor inversion (blue); the former approach may have larger uncertainty in fault plane orientations. Eight $M_L > 3$ events occurred between November and December 2016, seven of which have focal mechanism solutions, as presented. (b) A model showing vertical fault(s) and flower structure along the N–S orientation as suggested by Berger & Davies (1999). The directions of motion on the suggested fault (red solid arrows) and auxiliary (red dash arrows) planes from the swarm investigated in this study are as indicated.

5 DISCUSSION

Utilizing regional 3-component seismic data, we obtain a moment magnitude **M**4.1 for the J12EQ near Crooked Lake, which is consistent with the value from SLU (**M** = 4.14) but significantly lower than a reported M_L of 4.8 (AGS). Using moment tensor inversion, we are able to determine the moment magnitudes of a number of HF induced (or potentially induced) earthquakes in this region, including: **M** ∼ 3.5 in late 2013 and 2014, **M**3.6 ∼ 4.1 in 2015–2017. Despite the differences in magnitude scales reported by various agencies, the self-consistent solutions from moment tensor inversions rank the J12EQ the second largest in Alberta in the past 30 years, surpassed only by a suspected natural **M**5.2 earthquake near Dawson Creek in 2001 (Ristau *et al.* 2007; Earthquakes Canada). Until April, 2017 (Fig. 6), the J12EQ is also known to be the second largest HF induced earthquake in Canada, following

the **M**4.6 earthquake in August 2015 in the northeastern British Columbia (Babaie Mahani *et al.* 2017). The updated injection volume (30 998 m^3) falls within the uncertainties provided by fig. 4 of Atkinson *et al.* (2016). However, it is considerably larger than their estimated value (∼10 000 m^3, Atkinson *et al.* 2016) and leads to a predicted magnitude (**M**4.0, assuming a shear modulus of 40 GPa) that follows the linear relationship proposed by McGarr (2014).

Aside from magnitude, the source analysis of the J12EQ provides critical new information on the faulting and the state of crustal stress beneath the Fox Creek/Crooked Lake region. The preferred location of this earthquake is SW of Crooked Lake (Fig. 2), within one of the most active and highly publicized seismogenic zones in connection with HF operations. The shallowest depth of the January 2016 swarm overlaps with the HF injection depth at ∼3.5 km, which is further supported by the resolved depth from double-difference relocation analysis (Schultz *et al.* 2017). The largest estimated depth of the hypocentre is ∼4.3 km, potentially extending into the basement (3.8 km, Pilkington *et al.* 2000; Majorowicz *et al.* 2014).

Our focal mechanism analysis of the J12EQ suggests candidate fault planes in the N-S and E-W orientations (Fig. 2b), similar to the January 2015 events (Bao & Eaton 2016) and the first red-light event in June 2015 (Wang *et al.* 2016; Schultz *et al.* 2017). The P-axes from all **M** > 3 events near Fox Creek (Fig. 6a) are roughly parallel to the maximum compressive horizontal stress orientations (Fig. 1). Based on the possible rupture depth and orientations from the dominant strike-slip mechanism, we propose a model of the fault system for the January 2016 swarm as well as other earthquakes near Crooked Lake in recent years (Fig. 6). The suggested fault orientations are consistent with earlier findings from aeromagnetic data near Fox Creek, which provide compelling evidence for the Pine Creek fault zone with right-lateral strike-slip motions (Berger & Davies 1999). According to Berger & Davies (1999) and Berger & Zaitlin (2011), this fault system originated as N−S strike-slips in the basement and extend vertically into the sedimentary strata, showing a flower structure. The presence of basement faults in this region has been argued to have influenced the contour of some reef margins, which coincide with the spatial distribution of induced seismicity (Schultz *et al.* 2016).

Moment tensor analysis offers more constraints on the characteristics of the subsurface fault system (e.g. Skoumal *et al.* 2015). For an **M** ∼ 4 earthquake ascribed to a simple linear fault plane model, the size of the vertical fault area could be as small as 1 km^2 (Schultz *et al.* 2017). In contrast, the horizontal offsets of the deep-seated vertical faults could be as large as 2–3 km (Berger & Davies 1999), resulting in much larger fault areas capable of producing moderate-sized earthquakes (**M**3.8–5.8, Hanks & Kanomori 1979; Wells & Coppersmith 1994). For example, a ∼15 km long, N−S-trending fault has been reported near the Simonette region (∼10 km east of Crooked Lake) based on seismic reflection data (Cortis *et al.* 1997), as well as a graben at the depth of 3.1–3.8 km within the sedimentary layers (Green & Mountjoy 2005; Wang *et al.* 2016). In view of proximity of these faults to the location of the J12EQ, it is plausible that the wrench faults within the Pine Creek fault zone share similar origins and geometries. These faults served as effective conduits for fluid flow that facilitated the formation of dolomite-hosted gas reservoirs (Mountjoy *et al.* 1999; Duggan *et al.* 2001; Davies & Smith 2006). Considering the uncertainties of the hypocentral depth and the size of fault plane, it is difficult to determine whether the **M** ∼ 4 earthquakes occurred on faults within the basement or the overlying sedimentary strata. The triggering process could be linked to fluid migration along the shallower fractures and the reactivation of faults in/above the crystalline basement (Chopra et al. 2017). This mechanism was earlier suggested for earthquakes induced by wastewater disposal in North America (Ellsworth 2013; Rubinstein *et al.* 2014).

The 2016 Crooked Lake earthquake swarm detected from the four near-source industry stations offers further insight on the fault location and orientation of the J12EQ. This swarm resides within 1 km south of the reported induced seismic cluster from 2015 (Bao & Eaton 2016; Fig. 5). Most of the detected events (1065 out of 1108) are distributed parallel to a single HF well (dash box in Fig. 5) with an N-S trend, and are spatially separated from other wells in this region (Fig. 3). There is no apparent time-dependent spatial pattern during or after injection; for instance, the centre of the earthquakes during the post completion phase (after January 12) is only ∼100 m away from the events during the HF stimulation, which is smaller than the size of our search grid. The best-fit strike orientation for the seismic swarm (Fig. 5) is 202.64°, comparable to one of our fault plane orientations (184°) resolved from focal mechanism analysis. This trend is consistent with the double-difference relocation outcomes from Schultz *et al.* (2017), in which 92 small magnitude events were detected and relocated. Furthermore, both analyses located the earthquake swarm above the basement (depth = 3.8 km), leaving only a limited number of events within the top 1 km of the basement. Based on all the evidence above, we conclude that the January 2016 earthquake sequence is induced by the nearby horizontal well completion and the true fault orientation is N–S.

The best moment tensor solution is dominated by DC component (∼75 per cent), irrespective of the choice of the starting epicentre during the inversion (Fig. 2b). Our moment tensor solution shows limited dependence on the crustal velocity and attenuation model (Wang *et al.* 2016), as well as on station distribution (Fig. 3). The resolved moment tensor and the corresponding fault orientations are consistent with the solution of a pure-DC moment tensor inversion from SLU and our DC forward models, comparable to those of some other HF induced earthquake in the U.S. (e.g. McNamara *et al.* 2015; Skoumal *et al.* 2015). Our focal mechanism, as well as its decomposition, is highly consistent with that of the June 13, 2015 earthquake (Fig. 2b). Strike-slip dominated mechanisms with limited non-DC component are further resolved from several **M** > 3 earthquakes between 2015 and 2017 within the Fox Creek/Crooked Lake region (Fig. 6a). The similarity in focal depths, moment tensors, and their decomposition results suggest comparable triggering mechanisms for events associated with HF operations in this general area (Fig. 2b). Based on the moment tensor solutions of several events in western Canada, Zhang *et al.* (2016) suggests that, (1) shallower depths and (2) larger non-DC components are expected from induced earthquakes than natural earthquakes. Our analysis of the January 2016 earthquake swarm favours relatively shallow source depths, consistent with their first metric. However, the modest non-DC component based on improved crustal model and revised source location do not systematically differ from those of natural earthquakes (Cesca *et al.* 2013; Zhang *et al.* 2016). Such limited amount of non-DC component is also observed from HF induced events in the northern British Columbia (Babaie Mahani *et al.* 2017). Likely, resolving non-DC components with fidelity will require more data and a precise structure model (i.e. 3-D), as our experiments show that hypocentral biases, anisotropy and/or insufficient station coverage preferentially contribute to errors in the non-DC components (e.g. Frohlich 1994; Vavryčuk *et al.* 2008; Šílený *et al.* 2009; Wang *et al.* 2016).

6 CONCLUSIONS

The main purpose of this study is to present the source analysis of an HF induced seismic swarm during January 2016, especially the **M**4.1 earthquake, which is one of the largest earthquakes induced by HF operations worldwide. We are able to verify the J12EQ to be the largest earthquake in the past decade in Alberta through moment tensor inversions. This earthquake is dominated by the DC component, while source solutions are relatively independent of the initial hypocentral location. We further resolve several recent (2015–2017) earthquakes with similar strike-slip mechanisms in the Crooked Lake region. With more than a thousand events detected, the significance of the J12EQ is highlighted by the close spatial-temporal relationship to an HF well targeting the Duvernay Formation. The majority of the swarm took place during HF stimulation and the largest event occurred during the last stage of injection. The depth of the detected and located earthquake swarm is near the top of the crystalline basement and suggests the reactivation of an N-S-trending fault analogous to the Pine Creek fault zone.

ACKNOWLEDGEMENTS

The authors are grateful to Natural Resources Canada, Nanometrics, Saint Louis University Earthquake Center, National Earthquake Information Center and Alberta Geological Survey for the preliminary earthquake information. This paper benefited significantly from the reviews by Ivan Wong and three anonymous reviewers. We thank Gail Atkinson and Yunfeng Chen for helpful discussions and suggestions. Data from RAVEN and TD stations were requested through the Incorporated Research Institutions for Seismology (IRIS); the TD stations are contributed to IRIS by TransAlta. Moment tensors were computed using the tdmt-invc-iso package developed by Douglas Dreger and Sean Ford of the Berkeley Seismological Laboratory, and Green's functions were computed using the FKRPROG software developed by Chandan Saikia. Some figures in this paper were generated using the Generic Mapping Tool (Wessel *et al.* 2013). All presented focal mechanism solutions can be requested from the corresponding author.

REFERENCES

Alberta Energy Regulator, 2015. 'Subsurface order 2'. Available at: https://aer.ca/documents/orders/subsurface-orders/SO2.pdf, last accessed May 2017.

Atkinson, G.M., Greig, D.W. & Yenier, E., 2014. Estimation of moment magnitude (**M**) for small events (**M** < 4) on local networks, *Seismol. Res. Lett.,* **85**(5), 1116–1124.

Atkinson, G.M. *et al.*, 2016. Hydraulic fracturing and seismicity in the Western Canada Sedimentary Basin, *Seismol. Res. Lett.*, **87**(3), 631–647.

Babaie Mahani, A., Schultz, R., Kao, H., Walker, D., Johnson, J. & Salas, C., 2017. Fluid injection and seismic activity in the northern Montney play, British Columbia, Canada, with special reference to the 17 August 2015 M_w 4.6 induced earthquake, *Bull. seism. Soc. Am.*, doi:10.1785/0120160175.

Bao, X. & Eaton, D.W., 2016. Fault activation by hydraulic fracturing in western Canada, *Science*, **354**, 1406–1409

BC Oil and Gas Commission, 2012. 'Investigation of observed seismicity in the Horn River Basin'. Available at: https://www.bcogc.ca/node/8046/download, last accessed May 2017.

BC Oil and Gas Commission, 2014. 'Investigation of observed seismicity in the Montney Trend'. Available at: https://www.bcogc.ca/node/12291/download, last accessed May 2017.

Berger, Z. & Davies, G.R., 1999. The development of linear hydrothermal dolomite (HTD) reservoir facies along wrench or strike slip fault systems in the Western Canada Sedimentary Basin, *Can. Soc. Pet. Geologists Reservoir*, **26**(1), 34–38.

Berger, Z. & Zaitlin, B.A., 2011. Detection and analysis of structurally controlled enhanced reservoir potential in mature and emerging oil resource plays in the WCSB: tight oil examples from the Nordegg and Alberta Bakken, in *2011 CSPG CSEG CWLS Convention* Available at: http://www.geoconvention.com/archives/2011/252-Analysis_of_Structurally_Controlled_Enhanced_Reservoir_Potential.pdf, last accessed May 2017.

CBC news, 2016. 'Fox Creek fracking operation closed indefinitely after earthquake'. Available at: http://www.cbc.ca/news/canada/edmonton/fox-creek-fracking-operation-closed-indefinitely-after-earthquake-1.3400605, last accessed May 2017.

Cesca, S., Rohr, A. & Dahm, T., 2013. Discrimination of induced seismicity by full moment tensor inversion and decomposition, *J. Seismol.*, **17**(1), 147–163.

Chen, Y., Gu, Y.J., Dokht, R.M. & Sacchi, M.D., 2015. Crustal imprints of Precambrian orogenesis in western Laurentia, *J. geophys. Res.*, **120**, 5051–5069.

Chopra, S., Sharma, R.K., Ray, A.K., Nemati, H., Morin, R., Schulte, B. & D'Amico, D., 2017. Seismic reservoir characterization of Duvernay shale with quantitative interpretation and induced seismicity considerations–a case study, *Interpretation*, **5**(2), T185–T197.

Clerc, F., Harrington, R.M., Liu, Y. & Gu, Y.J., 2016. Stress drop estimates and hypocenter relocations of induced seismicity near Crooked Lake, Alberta, *Geophys. Res. Lett.*, **43**(13), 6942–6951.

Cortis, A., Ollenberger, L. & Fawcett, M., 1997. Simonette Beaverhill Lake oil field: a multi-cyclic approach to understanding reef growth and reservoir heterogeneity, in *CSPG-SEPM Joint Convention*, Calgary, Alberta, pp. 73–88.

Dahm, T. *et al.*, 2013. Recommendation for the discrimination of human-related and natural seismicity, *J. Seismol.*, **17**(1), 197–202.

Davies, G.R. & Smith, L.B., Jr., 2006. Structurally controlled hydrothermal dolomite reservoir facies: An overview, *AAPG Bull.*, **90**(11), 1641–1690.

Davis, M. & Karlen, G., 2013. A regional assessment of the Duvernay Formation; a world-class liquids-rich shale play, *GeoConvention: Integration, Calgary*, 6–10.

Deng, K., Liu, Y. & Harrington, R.M., 2016. Poroelastic stress triggering of the December 2013 Crooked Lake, Alberta, induced seismicity sequence, *Geophys. Res. Lett.*, **43**(16), 8482–8491.

Dreger, D.S., 2003. TDMT_INV: Time domain seismic moment tensor inversion, in *International Handbook of Earthquake and Engineering Seismology*, Part B, p. 1627, eds Lee, W.H.K., Kanamori, H., Jennings, P.C., Kisslinger, C., Academic Press, New York.

Duggan, J.P., Mountjoy, E.W. & Stasiuk, L.D., 2001. Fault-controlled dolomitization at Swan Hills Simonette oil field (Devonian), deep basin west-central Alberta, Canada, *Sedimentology*, **48**(2), 301–323.

Dunn, L. *et al.*, 2012. The Duvernay formation (Devonian): sedimentology and reservoir characterization of a shale gas/liquids play in Alberta, Canada, in *Canadian Society of Petroleum Geologists, Annual Convention, Calgary*, Available at: http://www.cspg.org/documents/Conventions/Archives/Annual/2012/core/280_GC2012_The_Duvernay_Formation.pdf, last accessed May 2017.

Efron, B. & Tibshirani, R., 1991. Statistical data analysis in the computer age, *Science*, **253**(5018), 390–395.

Ellsworth, W.L., 2013. Injection-induced earthquakes, *Science*, **341**, 6142, doi:10.1126/science.1225942.

Earthquakes Canada, http://earthquakescanada.nrcan.gc.ca/stndon/, last accessed February 2017.

Fan, W. & Shearer, P.M., 2016. Local near instantaneously dynamically triggered aftershocks of large earthquakes, *Science*, **353**(6304), 1133–1136.

Fouch, M.J. & Rondenay, S., 2006. Seismic anisotropy beneath stable continental interiors, *Phys. Earth planet. Inter.*, **158**(2), 292–320.

Fox, D.A. & Soltanzadeh, M., 2015. A regional geomechanical study of the Duvernay Formation in Alberta, Canada, *GeoConvention 2015: New Horizons*, Calgary, Alberta, May 4–8.

Frohlich, C., 1994. Earthquakes with non-double-couple mechanisms, *Science*, **264**(5160), 804–809.

Ghofrani, H. & Atkinson, G.N., 2016. A preliminary statistical model for hydraulic fracture-induced seismicity in the Western Canada Sedimentary Basin (WCSB), *Geophys. Res. Lett.*, **43**, doi:10.1002/2016GL070042.

Globalnews, 2016. 'Fox Creek mayor concerned by oilpatch impacts after earthquake', Available at: http://globalnews.ca/news/2452038/fox-creek-mayor-concerned-by-oilpatch-impacts-after-earthquake/, last accessed May 2017.

Green, D.G. & Mountjoy, E.W., 2005. Fault and conduit controlled burial dolomitization of the Devonian west-central Alberta Deep Basin, *Bull. Can. Pet. Geol.*, **53**(2), 101–129.

Gu, Y.J., Okeler, A., Shen, L. & Contenti, S., 2011. The Canadian Rockies and Alberta Network (CRANE): new constraints on the Rockies and Western Canada sedimentary basin, *Seismol. Res. Lett.*, **82**(4), 575–588.

Hanks, T. & Kanamori, H., 1979. A magnitude moment scale, *J. geophys. Res.*, **84**, 2348–2351.

Holland, A.A., 2013. Earthquakes triggered by hydraulic fracturing in south-central Oklahoma, *Bull. seism. Soc. Am.*, **103**(3), 1784–1792.

Kim, Y., Liu, Q. & Tromp, J., 2011. Adjoint centroid-moment tensor inversions, *Geophys. J. Int.*, **186**(1), 264–278.

Majorowicz, J. *et al.*, 2014. The first deep heat flow determination in crystalline basement rocks beneath the Western Canadian Sedimentary Basin, *Geophys. J. Int.*, **197**(2), 731–747.

McGarr, A., 2014. Maximum magnitude earthquakes induced by fluid injection, *J. geophys. Res.*, **119**, 1008–1019.

McNamara, D.E., Benz, H.M., Herrmann, R.B., Bergman, E.A., Earle, P., Holland, A., Baldwin, R. & Gassner, A., 2015. Earthquake hypocenters and focal mechanisms in central Oklahoma reveal a complex system of reactivated subsurface strike-slip faulting, *Geophys. Res. Lett.*, **42**(8), 2742–2749.

Mountjoy, E.W., Machel, H.G., Green, D., Duggan, J. & Williams-Jones, A.E., 1999. Devonian matrix dolomites and deep burial carbonate cements: a comparison between the Rimbey-Meadowbrook reef trend and the deep basin of west-central Alberta, *Bull. Can. Pet. Geol.*, **47**(4), 487–509.

Ong, O.N., Schmitt, D.R., Kofman, R.S. & Haug, K., 2016. Static and dynamic pressure sensitivity anisotropy of a calcareous shale, *Geophys. Prospect.*, **64**(4), 875–897.

Pilkington, M., Miles, W.F., Ross, G.M. & Roest, W.R., 2000. Potential-field signatures of buried Precambrian basement in the Western Canada Sedimentary Basin, *Can. J. Earth Sci.*, **37**(11), 1453–1471.

Ristau, J., Rogers, G.C. & Cassidy, J.F., 2007. Stress in western Canada from regional moment tensor analysis, *Can. J. Earth Sci.*, **44**(2), 127–148.

Rokosh, C.D. *et al.*, 2012. Summary of Alberta's Shale-and Siltstone-Hosted Hydrocarbons, *ERCB/AGS Open File Report,* **6**.

Rubinstein, J.L. & Mahani, A.B., 2015. Myths and facts on wastewater injection, hydraulic fracturing, enhanced oil recovery, and induced seismicity, *Seismol. Res. Lett*, **86**(4), 1060–1067.

Rubinstein, J.L., Ellsworth, W.L., McGarr, A. & Benz, H.M., 2014. The 2001-present induced earthquake sequence in the Raton Basin of northern New Mexico and southern Colorado, *Bull. seism. Soc. Am.*, **104**(5), 2162–2181.

Saikia, C.K., 1994, Modified frequency-wavenumber algorithm for regional seismograms using Filon's quadrature: modelling of Lg waves in eastern North America, *Geophys. J. Int.*, **118**(1), 142–158.

Saruwatari, K., Ji, S., Long, C. & Salisbury, M.H., 2001. Seismic anisotropy of mantle xenoliths and constraints on upper mantle structure beneath the southern Canadian Cordillera, *Tectonophysics*, **339**(3), 403–426.

Schultz, R. & Stern, V., 2015. The Regional Alberta Observatory for Earthquake Studies Network (RAVEN), *CSEG Recorder*, **40**(8), 34–37.

Schultz, R., Stern, V. & Gu, Y.J., 2014, An investigation of seismicity clustered near the Cordel Field, west central Alberta, and its relation to a nearby disposal well, *J. geophys. Res.*, **119**, 3410–3423.

Schultz, R., Mei, S., Pană, D., Stern, V., Gu, Y.J., Kim, A. & Eaton, D., 2015a. The Cardston earthquake swarm and hydraulic fracturing of the Exshaw Formation (Alberta Bakken play), *Bull. seism. Soc. Am.*, **105**(6), 2871–2884.

Schultz, R., Stern, V., Novakovic, M., Atkinson, G. & Gu, Y.J., 2015b. Hydraulic fracturing and the Crooked Lake sequences: insights gleaned from regional seismic networks, *Geophys. Res. Lett.*, **42**, 2750–2758.

Schultz, R., Corlett, H., Haug, K., Kocon, K., MacCormack, K., Stern, V. & Shipman, T., 2016. Linking fossil reefs with earthquakes: geologic insight to where induced seismicity occurs in Alberta, *Geophys. Res. Lett.*, **43**, 2534–2542.

Schultz, R., Wang, R., Gu, Y.J., Hang, K. & Atkinson, G., 2017. A seismological overview of the induced seismicity in the Duvernay play near Fox Creek, Alberta, *J. geophys. Res.*, **22**, 492–505.

Šílený, J., Hill, D.P., Eisner, L. & Cornet, F.H., 2009. Non–double-couple mechanisms of microearthquakes induced by hydraulic fracturing, *J. geophys. Res.*, **114**, B08307, doi:10.1029/2008JB005987.

Skoumal, R.J., Brudzinski, M.R. & Currie, B.S., 2015. Earthquakes induced by hydraulic fracturing in Poland Township, Ohio, *Bull. seism. Soc. Am.*, **105**(1), 189–197.

Switzer, S.B., Holland, W.G., Christie, D.S., Graf, G.C., Hedinger, A.S., McAuley, R.J., Wierzbicki, R.A. & Packard, J.J., 1994. Devonian woodbend-winterburn strata of the Western Canada Sedimentary Basin, in *Atlas of the Western Canada Sedimentary Basin*, pp. 165–202, eds Mossop, G.D. & Shetsen, I., Canadian Society of Petroleum Geologists and Alberta Research Council.

Telesca, L., 2010. Analysis of the cross-correlation between seismicity and water level in the Koyna area of India, *Bull. seism. Soc. Am.*, **100**(5A), 2317–2321.

Udías, A., Madariaga, R. & Buforn, E., 2014. Determination of point source mechanisms, in *Source Mechanisms of Earthquakes: Theory and Practice,* Cambridge Univ. Press. Chap. 6, pp. 108–133.

Vavryčuk, V., Bohnhoff, M., Jechumtálová, Z., Kolář, P. & Šílený, J., 2008. Non-double-couple mechanisms of microearthquakes induced during the 2000 injection experiment at the KTB site, Germany: A result of tensile faulting or anisotropy of a rock?, *Tectonophysics*, **456**(1), 74–93.

Wang, B., Harrington, R.M., Liu, Y., Yu, H., Carey, A. & Elst, N.J., 2015. Isolated cases of remote dynamic triggering in Canada detected using cataloged earthquakes combined with a matched-filter approach, *Geophys. Res. Lett.*, **42**(13), 5187–5196.

Wang, R., Gu, Y.J., Schultz, R., Kim, A. & Atkinson, G., 2016. Source analysis of a potential hydraulic-fracturing-induced earthquake near Fox Creek, Alberta, *Geophys. Res. Lett.*, **43**, doi:10.1002/2015GL066917.

Welford, J.K. & Clowes, R.M., 2006. Three-dimensional seismic reflection investigation of the upper crustal Winagami sill complex of northwestern Alberta, Canada, *Geophys. J. Int.*, **166**(1), 155–169.

Wells, D.L. & Coppersmith, K.J., 1994. New empirical relationships among magnitude, rupture length, rupture width, rupture area, and surface displacement, *Bull. seism. Soc. Am.*, **84**(4), 974–1002.

Wendte, J. & Uyeno, T., 2005. Sequence stratigraphy and evolution of Middle to Upper Devonian Beaverhill Lake strata, south-central Alberta, *Bull. Can. Pet. Geol.*, **53**(3), 250–354.

Wessel, P., Smith, W.H.F., Scharroo, R., Luis, J.F. & Wobbe, F., 2013. Generic Mapping Tools: improved version released, *EOS, Trans. Am. geophys. Un.*, **94**, 409–410.

Wetmiller, R.J., 1986. Earthquakes near Rocky Mountain House, Alberta, and their relationship to gas production facilities, *Can. J. Earth Sci.*, **23**(2), 172–181.

Zelt, C. & Ellis, R., 1990. Crust and upper mantle Q from seismic refraction data: Peace River region, *Can. J. Earth Sci.*, **27**(8), 1040–1047.

Zhang, M. & Wen, L., 2015a. An effective method for small event detection: match and locate (M&L), *Geophys. J. Int.*, **200**(3), 1523–1537.

Zhang, M. & Wen, L., 2015b. Earthquake characteristics before eruptions of Japan's Ontake volcano in 2007 and 2014, *Geophys. Res. Lett.*, **42**(17), 6982–6988.

Zhang, H., Eaton, D.W., Li, G., Liu, Y. & Harrington, R.M. 2016. Discriminating induced seismicity from natural earthquakes using moment tensors and source spectra, *J. geophys. Res.*, **121**, 972–993.

SUPPORTING INFORMATION

Supplementary data are available at *GJI* online.

Figure S1. A comparison of focal mechanisms before (bottom) and after (top) secondary shifts are applied to individual components of each near-source station (<250 km).

Figure S2. Example of the fitted waveform from a near-source station (TD002). The high-frequency body-wave waveforms are shown on the left and the low-frequency surface-wave waveforms are shown on the right. The waveforms of observed data are shown in dark grey and the red/dash lines show the synthetic data after/before applying secondary shifts to correct the possible effect of anisotropy.

Table S1. Variance reduction (see eq. 1) values and moment tensor decomposition (displayed as double-couple/compensated-linear-vector-dipole/isotropic) for different hypocentre locations before and after the correction for individual components. The preferred solution is coloured in red. The names and locations of the agencies are shown in Fig. 1.